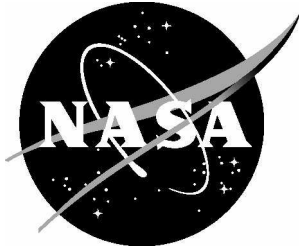


NASA/TP-2006-214533



A Dynamic/Anisotropic Low Earth Orbit (LEO) Ionizing Radiation Model

Francis F. Badavi
Christopher Newport University, Newport News, Virginia

Katie J. West
Duke University, Durham, North Carolina

John E. Nealy
Old Dominion University, Norfolk, Virginia

John W. Wilson
NASA Langley Research Center, Hampton, Virginia

Briana L. Abrahms
Brandeis University, Waltham, Massachusetts

Nathan J. Luetke
Lockheed Martin, Hampton, Virginia

December 2006

The NASA STI Program Office . . . in Profile

Since its founding, NASA has been dedicated to the advancement of aeronautics and space science. The NASA Scientific and Technical Information (STI) Program Office plays a key part in helping NASA maintain this important role.

The NASA STI Program Office is operated by Langley Research Center, the lead center for NASA's scientific and technical information. The NASA STI Program Office provides access to the NASA STI Database, the largest collection of aeronautical and space science STI in the world. The Program Office is also NASA's institutional mechanism for disseminating the results of its research and development activities. These results are published by NASA in the NASA STI Report Series, which includes the following report types:

- **TECHNICAL PUBLICATION.** Reports of completed research or a major significant phase of research that present the results of NASA programs and include extensive data or theoretical analysis. Includes compilations of significant scientific and technical data and information deemed to be of continuing reference value. NASA counterpart of peer-reviewed formal professional papers, but having less stringent limitations on manuscript length and extent of graphic presentations.
- **TECHNICAL MEMORANDUM.** Scientific and technical findings that are preliminary or of specialized interest, e.g., quick release reports, working papers, and bibliographies that contain minimal annotation. Does not contain extensive analysis.
- **CONTRACTOR REPORT.** Scientific and technical findings by NASA-sponsored contractors and grantees.

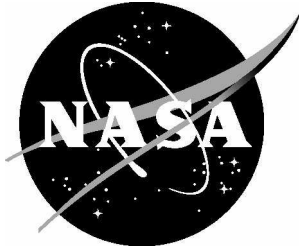
- **CONFERENCE PUBLICATION.** Collected papers from scientific and technical conferences, symposia, seminars, or other meetings sponsored or co-sponsored by NASA.
- **SPECIAL PUBLICATION.** Scientific, technical, or historical information from NASA programs, projects, and missions, often concerned with subjects having substantial public interest.
- **TECHNICAL TRANSLATION.** English-language translations of foreign scientific and technical material pertinent to NASA's mission.

Specialized services that complement the STI Program Office's diverse offerings include creating custom thesauri, building customized databases, organizing and publishing research results ... even providing videos.

For more information about the NASA STI Program Office, see the following:

- Access the NASA STI Program Home Page at <http://www.sti.nasa.gov>
- E-mail your question via the Internet to help@sti.nasa.gov
- Fax your question to the NASA STI Help Desk at (301) 621-0134
- Phone the NASA STI Help Desk at (301) 621-0390
- Write to:
NASA STI Help Desk
NASA Center for AeroSpace Information
7115 Standard Drive
Hanover, MD 21076-1320

NASA/TP-2006-214533



A Dynamic/Anisotropic Low Earth Orbit (LEO) Ionizing Radiation Model

Francis F. Badavi
Christopher Newport University, Newport News, Virginia

Katie J. West
Duke University, Durham, North Carolina

John E. Nealy
Old Dominion University, Norfolk, Virginia

John W. Wilson
NASA Langley Research Center, Hampton, Virginia

Briana L. Abrahms
Brandeis University, Waltham, Massachusetts

Nathan J. Luetke
Lockheed Martin, Hampton, Virginia

National Aeronautics and
Space Administration

Langley Research Center
Hampton, Virginia 23681-2199

December 2006

Available from:

NASA Center for AeroSpace Information (CASI)
7115 Standard Drive
Hanover, MD 21076-1320
(301) 621-0390

National Technical Information Service (NTIS)
5285 Port Royal Road
Springfield, VA 22161-2171
(703) 605-6000

A Dynamic/Anisotropic Low Earth Orbit (LEO) Ionizing Radiation Model

Francis F. Badavi¹, Katie J. West², John E. Nealy³, John W. Wilson⁴,
Briana L. Abrahms⁵, Nathan J. Luetke⁶

¹*Christopher Newport University, Newport News, VA., 23606*

²*Duke University, Durham, NC., 27708*

³*Old Dominion University, Norfolk, VA., 23685*

⁴*NASA Langley Research Center, Hampton, VA., 23681*

⁵*Brandeis University, Waltham, MA., 02454*

⁶*Lockheed Martin, Hampton, VA., 23681*

The International Space Station (ISS) provides the proving ground for future long duration human activities in space. Ionizing radiation measurements in ISS form the ideal tool for the experimental validation of ionizing radiation environmental models, nuclear transport code algorithms, and nuclear reaction cross sections. Indeed, prior measurements on the Space Transportation System (STS; Shuttle) have provided vital information impacting both the environmental models and the nuclear transport code development by requiring dynamic models of the Low Earth Orbit (LEO) environment. Previous studies using Computer Aided Design (CAD) models of the evolving ISS configurations with Thermo Luminescent Detector (TLD) area monitors, demonstrated that computational dosimetry requires environmental models with accurate non-isotropic as well as dynamic behavior, detailed information on rack loading, and an accurate 6 degree of freedom (DOF) description of ISS trajectory and orientation. It is imperative that we understand ISS exposures dynamically for crew career planning, and insure that the regulatory requirements of keeping exposure as low as reasonably achievable (ALARA) are adequately implemented. This is especially true as ISS nears some form of completion with increasing complexity, resulting in a larger drag coefficient, and requiring operation at higher altitudes with increased exposure rates. The ISS environmental model is now configured for 11A, and uses non-isotropic and dynamic geomagnetic transmission and trapped proton models. ISS 11A and LEO model validations are important steps in preparation for the design and validation of the Crew Exploration Vehicle (CEV) under the Constellation program. We describe herein improved ionizing radiation environmental models of trapped proton and Galactic Cosmic Ray (GCR) as applied in ISS operations. We further apply these environmental models to selected target points within ISS 6A, 7A, and 11A, during its passage through the South Atlantic Anomaly (SAA) to assess the validity of the environmental models.

Nomenclature

ALARA	= As Low As Reasonably Achievable
AP8MIN	= Aerospace Corp. proton unified field model-1965 (rev. 8)
AP8MAX	= Aerospace Corp. proton unified field model-1970 (rev. 8)
a_p	= Coefficient in trapped proton flux parameterization
B	= Magnetic flux density
C_D	= Magnitude of dipole moment
CAD	= Computer Aided Design
CEV	= Crew Exploration Vehicle
DOF	= Degree of freedom
DRNM	= Deep River Neutron Monitor
d_s	= Ionospheric scale height
E	= Proton kinetic energy
EVA	= Extra Vehicular Activity
F_N	= Normalization factor for the trapped proton directional distribution function
$F(F_{10.7})$	= 10.7 cm radio frequency solar index
\bar{F}	= Average of $F_{10.7}$ over three solar rotations
$f_p(r, \phi, \theta, E, t)$	= Time, energy, and directional dependent flux of trapped protons
GCR	= Galactic Cosmic Ray
GSFC	= Goddard Space Flight Center
H	= Altitude
ISS	= International Space Station
I	= Geomagnetic field dip angle
IGRF	= International Geomagnetic Reference Field
$J/J_{4\pi}$	= Ratio of directional proton flux to omni-directional (integrated) proton flux
KeV	= kilo electron Volt
LaRC	= Langley Research Center
LEO	= Low Earth Orbit
LV	= Local Vertical coordinate system
MeV	= Mega electron Volt
N, N_ϕ, N_θ	= Number of rays
NOAAPRO	= National Oceanic and Atmospheric Administration proton satellite measurements
NSSDC	= National Space Science Data Center
R	= Magnetic rigidity
R_{VC}	= Local vertical cutoff magnetic rigidity
r_D	= Distance from magnetic dipole center
r_E	= Earth radius
r_g	= Trapped proton gyroradius
SAA	= South Atlantic Anomaly
SC	= Spacecraft coordinate system
STS	= Space Transportation System (Shuttle)
Sv	= Sievert
TLD	= Thermo Luminescence Dosimeter
ζ	= Zenith angle
θ	= Pitch angle in the local vertical coordinate, also geographical latitude
ϕ	= Geographical longitude
λ_M	= Magnetic latitude
σ_θ	= Pitch angle standard deviation
ψ	= Azimuth angle in local vertical coordinate
ρ	= Atmospheric scale height
$\Delta\Omega$	= Element of solid angle
$\Delta\phi, \Delta\theta$	= Elements in the azimuth, and zenith direction

I. Introduction

The commitment of astronauts to the long term exposure of the space environment in ISS requires resolution of health issues directly related to the effects of ionizing radiation on the crew. Evidence of early cataract formation in STS operations¹ adds emphasis to the need for improving analysis and mitigation strategies of ionizing radiation. For the high inclination of ISS (51.6°), computational models indicate that about half of the ionizing radiation exposure near solar minimum results from GCR ($\approx 233 \mu\text{Sv/d}$), and the bulk of the remainder from trapped particles ($\approx 166 \mu\text{Sv/d}$)². For lightly shielded regions within ISS (e.g., in the crew quarters usually nested against the pressure vessel), the trapped particle exposure increases relative to GCR as the altitude of ISS increases to reduce atmospheric drag for the more advanced ISS configurations. Excluding the effects of the intervening material, there is also contribution from the neutron albedo³ of 25 - 54 $\mu\text{Sv/d}$ (varying with solar cycle). Within ISS, the ionizing radiation environment is a complex mixture of surviving primary particles and secondary radiations produced within the ISS structure. Various arrangements of detectors have been used to study the composition of the internal radiation fields within ISS, which needs to be understood to allow a more comprehensive modeling of the effects of the local radiation environment on the astronauts' critical tissues. As a result, a number of studies of various past spacecrafts within LEO environment have been made to better understand the nature of the ionizing radiations⁴⁻⁷, and to further understand these results in terms of computational models⁸⁻¹².

A prior report¹² used a relatively complete dynamic model based on simple scaling relations of the LEO environment as related to the solar activity cycle for the omni-directional flux of particles from GCR, trapped particles, and neutron albedo. In the present report, we first discuss the addition of directional dependency to this environment. In addition to the directional dependent trapped proton model, we also discuss the development of a directional dependent geomagnetic transmission model, with the understanding that the main effect of this dependency is the penetration of particles below the vertical transmission cutoff used in the past models.

The ISS, at the present time has evolved as a near Earth space habitat suitable for continuous human occupation. Further evolution of ISS should render it as a facility forming a vital part of an expanding space exploration infrastructure. The main motivation behind this work is to look at the ionizing radiation exposure aspects of astronaut health and safety by utilizing analytical procedures to determine ionizing radiation dose rates, with a view toward implementation as an analysis tool to facilitate the evaluation of the shield augmentation of the habitation modules. A CAD model of ISS 6A, 7A, and 11A configurations specifically dedicated to exposure analysis has been developed as part of this continuing study.

The first step in the analytical process begins with the establishment of an appropriate environmental model. For the LEO environment as applied to a pressurized vehicle, the most important contributors to the deposition of ionizing radiation energy are the trapped protons and GCR. The present study addresses first the highly directional (vectorial) proton flux, which roughly constitutes half of the total cumulative exposure for long duration missions. However, instantaneous dose rates are much higher during the approximately 10–15 minutes of the SAA transits, for which most of the trapped proton exposure occurs. During the transits, both omni-directional and vector proton flux vary from near zero to maximum values, and directionality is controlled by the vehicle orientation with respect to the magnetic field vector components. Consequently, an added degree of complexity is introduced with the time variation of proton flux spectra along the orbit, for which individual transport properties through the shield medium must be taken into account. The study then analyzes the directional dependent geomagnetic transmission due to the ever present GCR. The deterministic high energy heavy ion transport code HZETRN¹³, developed at NASA Langley Research Center (LaRC), is used to describe the attenuation and interaction of the LEO environment particles and to calculate dosimetric quantities of interest. The three ISS geometries defined by the CAD models are finally used to calculate exposures at selected target points within the modules, some of which represent locations of TLD detectors.

II. Analytical Description of Vector Flux in LEO

The two primary limitations in the environmental models described in reference 12 were the assumption that the trapped particles are isotropic (resulting from the omni-directional fluence description), and the use of the vertical geomagnetic cutoff to describe the transmitted GCR. These models have been relatively successful in describing the radiation environment aboard the highly maneuverable STS wherein anisotropies tend to be averaged (smeared) out. This averaging process is due to the fact that the spinning and random STS orientations wash out proton anisotropies, and hence directionality in the trapped proton flux is generally ignored for STS flights, with omni-directional fluxes being used for dosimetric calculations. Such models will not be adequate in the formation flying of ISS, which is mainly oriented in the local horizontal plane along the velocity vector. Presented here are the dynamic/anisotropic trapped proton environment and generalized geomagnetic cutoff models. These models are placed in a suitable form for evaluation of the incident radiation on the bounding surface of the 6 DOF motion described by longitude, latitude, and altitude (i.e., trajectory); and yaw, pitch, and roll (i.e., orientation) of an orbiting spacecraft. It must also be stated that even though both the trapped protons and GCR are positively charged, their directional behavior in the geomagnetic field are vastly different since GCR is incident on the magnetosphere with essentially isotropic flux, while trapped protons are largely introduced into the geomagnetic confining field from the underlying earth atmosphere. Hence, these constituents require somewhat different analytical approaches to describe their respective directional fluxes.

A. Trapped Proton Environment

The trapped proton population is traditionally modeled as AP8 for solar minimum and maximum¹⁴. These inner zone particles result from the decay of atmospheric neutrons as they leak from the Earth's atmosphere into the trapping region. The inner zone particles are lost from the trapping region by interaction with the tenuous atmosphere and generally have long trapping lifetimes. The inner zone consists of both proton and electron decay products. The average kinetic energy of the inner zone electrons is a few hundred keV. The electrons are easily removed from the spacecraft interior by the slightest amount of shielding, and are mainly of concern to an astronaut in a spacesuit during EVA, or for an externally mounted, lightly shielded electronics device. Within any pressure vessel such as STS or ISS, the electrons are easily shielded by the meteoroid/debris bumper and pressure vessel wall. Of the trapped particles, only the protons with energies near or above 50 MeV are of concern to the interior environment of STS or ISS.

The particles trapped in the geomagnetic field were modeled from data obtained during two epochs of solar cycle 20 (solar minimum of 1965 and solar maximum of 1970), and are used with the geomagnetic fields on which the B/L maps were prepared¹⁵. The 1965 analysis using the magnetic field model of Jensen and Cain¹⁶ resulted in the particle population maps AP8 MIN¹⁷. The 1970 analysis using the magnetic field model of GSFC 12/66¹⁸ extended to 1970, resulted in the particle population maps of AP8 MAX¹⁷. These models are considered the best global representations of the trapped proton environment.

It was believed at one time that better estimates of particle environments could be gained by evaluating the population maps defined on invariant McIlwain coordinates over current magnetic field conditions. This interpolation would, for example, contain the westward drift ($\sim 0.3^\circ$ W/yr.) of the SAA, observed in recent years by Badhwar et al.¹⁹. However, it was recognized by STS dosimetry group²⁰⁻²⁴ that large errors resulted from such a procedure and it was concluded that the use of the particle population maps interpolated over the magnetic field model for which the population map was derived would provide the best estimates of the long term orbit averaged particle environments even though the westward drift is not represented. It is now customary to introduce the westward drift as a rotation of geographic coordinates ($\sim 0.3^\circ$ /yr.) without modifying the magnetic field²⁵.

Since the principle source of trapped protons results from the neutron albedo of the atmosphere, the temporal behavior of the trapped proton population correlates with GCR intensity, and hence, solar activity. Figure 1 depicts the temporal variation of GCR and its inverse correlation with solar activity.

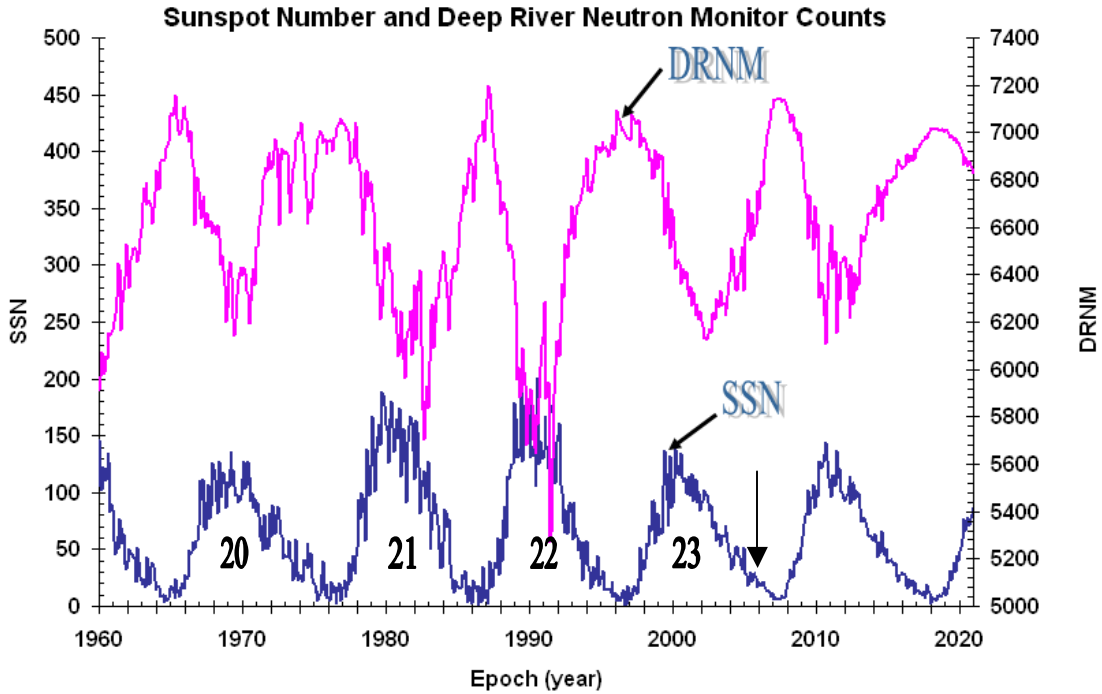


Figure 1. Temporal variation of solar activity (Sun spot number), and deep river neutron monitor counts.

Practically all of the trapped proton flux in LEO orbits (~300 - ~1000 km) is encountered in the SAA region. The flux exhibits pronounced directional characteristics, since this is a region close to a “mirror point” where the proton pitch angle with respect to the magnetic field vector is close to 90° . Within the SAA trapped protons attain their minimum mirror point altitudes, displaying planar geometry as their dominant feature. This means that the proton flux is maximized in the plane normal to the local magnetic field, which implies that at the point of observation protons that are not normal to the magnetic field are mirrored at lower altitudes while being heavily attenuated due to the increased interaction with the upper atmosphere.

The theoretical basis for the trapped flux directionality was initially developed by Heckman²⁶, who had studied the angular distribution of trapped protons with nuclear emulsion on rockets earlier, and presented a simple model of the pitch angle distributions about the geomagnetic field lines as related to the lifetimes of particles with guiding centers on different field lines²⁷. The protons’ velocity vectors lie within 15° of a plane perpendicular to the geomagnetic field line. Thus, those protons arriving from the east or the west differ in intensity according to the atmospheric scale height as related to the differences in population lifetime. This so called “east-west effect”, by which more protons arrive from the west direction than the east direction, is primarily due to the energy loss in the residual high altitude atmosphere. Simply stated, protons arriving from the west have trajectories with gyration about a point located above the reference observational point, and hence encounter less residual atmosphere. On the other hand, protons arriving from the east have trajectories with gyration about a point located below the reference observational point, and hence encounter more residual atmosphere. It is also well established that proton anisotropy is more pronounced at higher energies, where protons have a larger radius of gyration and thus can traverse through larger ranges of atmospheric densities. Limited measurements and models seem to indicate that, roughly

speaking, proton anisotropy is inversely proportional to the altitude, as atmospheric density gradients gradually diminish at higher altitudes.

After Heckman's initial work, some computational models were developed to analyze the effects of directionality^{28,29}. Using assumptions and approximations of reference 26, an expression for directional flux, J , can be expressed in terms of local magnetic field vector, B ; altitude, h ; ionosphere scale height, d_s ; and pitch and azimuth angles (θ and ψ , respectively). That is, for the direction of arrival, the directional intensity can be defined by the local pitch and azimuth angle pair θ, ψ . This formula, in the nomenclature of Kern²⁹, is expressed as a ratio of the vector flux to the omni-directional value, $J_{4\pi}$

$$\frac{J}{J_{4\pi}} = F_N \exp\left[\frac{-(\pi/2 - \theta)^2}{2\sigma_\theta^2}\right] \exp\left[\frac{r_g \cos I \cos \psi}{d_s}\right] \quad (1)$$

where I is the magnetic dip angle, and r_g is the proton gyro-radius, given (in km) by

$$r_g = \frac{\sin \theta \sqrt{E^2 + 1876E}}{30|\vec{B}|} \quad (2)$$

with the proton kinetic energy, E , in MeV and magnetic field strength, B , in gauss. The standard deviation of pitch angle, σ_θ is given by

$$\sigma_\theta = \sqrt{\frac{d_s}{K \sin I}} \quad (3)$$

where d_s is the ionospheric scale height and

$$K = (4/3) \frac{r_E + h}{(2 + \cos^2 I) \sin I} \quad (4)$$

with r_E representing the earth radius. F_N is a normalization factor, parameterized by Kern²⁹ as

$$F_N = (.075 / \sigma_\theta) (.8533 + x) e^{-x} \quad (5)$$

with

$$x = \frac{r_g \cos I}{d_s \sin \theta} \quad (6)$$

When the omni-directional flux is redistributed according to the distribution function of Equation (1), a pattern emerges in which most particles are directed in a very pronounced band of azimuth and zenith angles. Within the SAA, the pattern is concentrated around pitch angles near 90° and exhibit the aforementioned east-west asymmetry.

It was shown by Heckman and Nakano²⁶ that σ_θ in equations 1 and 3, depends on atmospheric scale height, altitude, and dip angle so that pitch angle distributions are nearly independent of particle energy. In

distinction, the east-west asymmetry depends on the particle radius of gyration, displaying marked energy dependency in azimuth. Figure 2, demonstrates the east-west asymmetry for 5 and 500 MeV protons. Due to the dependence of the asymmetry on the particle gyration, the asymmetry is noticeably pronounced for 500 MeV protons, while it is almost absent from the 5 MeV protons. The width of the band shown in the figure is determined by the pitch angle distribution.

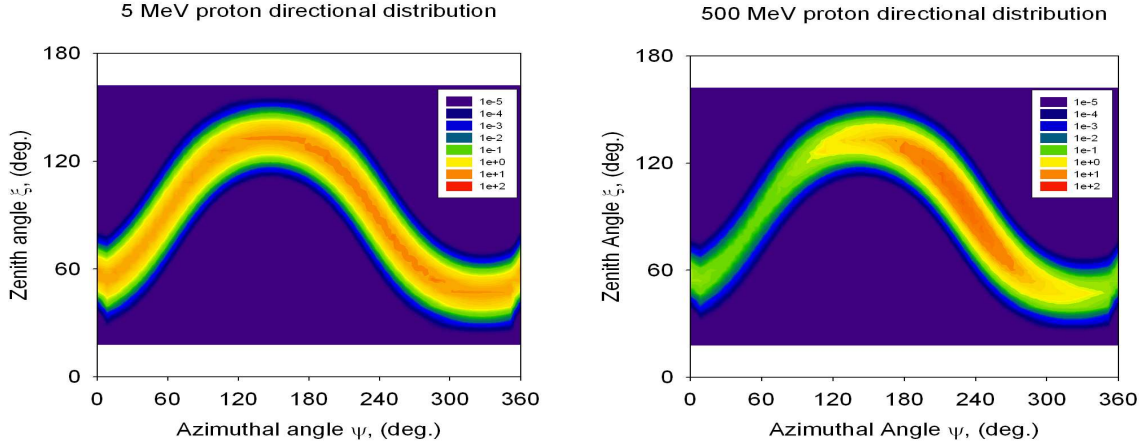


Figure 2. Directional dependence of trapped protons of 5 MeV (left), and 500 MeV (right) as viewed in the center of the SAA.

It must be stated that the IGRF fields, as implemented, drift the trapped field statically in a north-west direction at an approximate rate of 0.3° W/yr. and 0.04° N/yr. to the time of interest, and the scale height is found from the solar modulated fit of Pfitzer³⁰, as used by Badhwar³¹, to organize the STS dosimetry data, and is given by

$$\rho(r) = \rho_0 e^{\left(\frac{-(h-120)}{A(h-103)^{1/2}}\right)} \quad (7)$$

where $\rho_0 = 2.7 \times 10^{-11} \text{ g/cm}^3$, h is altitude above ground (in km), and fitting parameter A is defined as

$$A = 0.99 + .518[(F + \bar{F})/110]^{1/2} \quad (8)$$

with \bar{F} as the average of F over three prior solar rotations (81 days).

Due to orbital precession, the trapped protons as encountered by ISS during its 10-15 minutes passage through the SAA, encounter this region from both ascending and descending node directions. Because the radiation incident on the outer surface of the spacecraft is required for shield evaluation, and the attitude of the spacecraft is never fixed but has limited cycles due to the required reorientation maneuvers, the angular distribution averaged over spacecraft attitude in the region of radiation encounter needs to be evaluated. This is accomplished by relating the orientations in the spacecraft frame through yaw, pitch, and roll to the local vertical reference frame where the radiation environment is evaluated. In this work, 970 ray directions, as will be discussed in section III, are used to evaluate the boundary conditions for shield evaluation, and the same directions will be used for the evaluation of the directional environment. The region over which the environment is to be evaluated is typical of results shown in Figure 3.

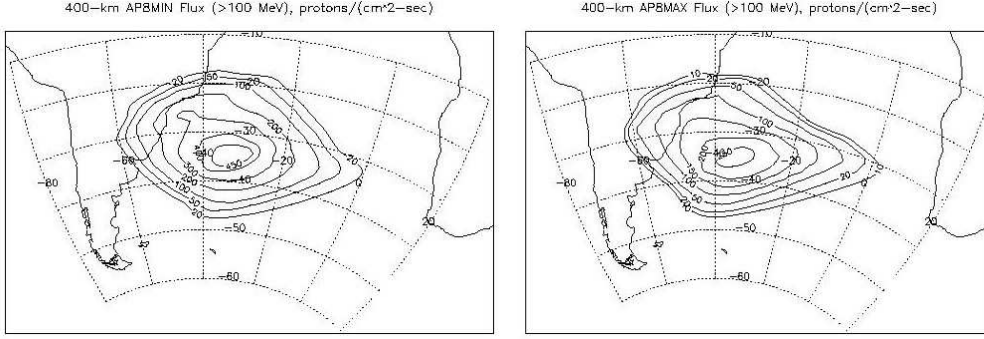


Figure 3. Location and integral flux of the SAA region for AP8 MIN-1965, and AP8 MAX-1970.

The trapped proton environment has as its source the neutron albedo, and losses which occur through atmospheric interactions. The proton environment is then proportional, in steady state, to the source (i.e., neutron albedo) and the population lifetime (i.e., atmospheric interaction), as was shown by Blanchard and Hess³². The interpolation procedure implemented here assumes a steady state solution to the population kinetic equations as the product of the albedo neutron source and the particle population lifetimes. These two quantities are proportional to the product of neutron monitor count rate and solar radio output at the 10.7 cm wavelength. The interpolation of the AP8 models then involves two operations. First is the shift of approximately 0.19° W/yr., 0.07° N/yr., and second, the solar modulation through the neutron decay source and loss terms due to the atmospheric interaction.

The AP8 MIN and AP8 MAX models associated with epochs 1965 and 1970 use different field models resulting in some artifacts in the data analysis that we have approximately corrected. The AP8 MIN and AP8 MAX locations of the SAA are given in Table 1. Here, based on the analysis of Atwell²¹, conventions in reference 25 are modified, and we assume a parametric fit for the location of the center of the SAA as a function of time, based on the following equations applicable to AP8 MAX of 1970 epoch:

$$\theta(t) = -32.2 + 0.07 * (t - 1970) \quad (9)$$

$$\phi(t) = -38 - 0.19 * (t - 1970) \quad (10)$$

Equations 9 and 10 assume a north-westward drift to properly locate the SAA associated with AP8 MAX, as given in Table 1, as the adjusted longitudinal values. Thus, $f_{AP8MAX}(r, \phi + 8, \theta - 4.8, E)$ as derived from AP8 MAX is adjusted by 4.8° N and 8° W, while assumed values for $f_{AP8MIN}(r, \phi + 4.1, \theta - 2.4, E)$ are those from AP8 MIN shifted by 2.4° N, and 4.1° W. A first approximation to the successive solar maximum and solar minimum is found by simply shifting north-westward the adjusted $f_{AP8MAX}(r, \phi + 8 + 0.19\Delta t, \theta - 4.8 - 0.07\Delta t, E)$ and $f_{AP8MIN}(r, \phi + 4.1 + 0.19\Delta t, \theta - 2.4 - 0.07\Delta t, E)$, where Δt is the time difference from time of evaluation to time of epoch for the AP8 data set.

SAA Location	Virgin model	Adjusted
1965		
Latitude	35.0°S	32.6°S
Longitude	33.0°W	37.1°W
1970		
Latitude	37.0°S	32.2°S
Longitude	30.0°W	38.0°W

Table 1. SAA Locations for 100 MeV Protons at 400 km during Epochs 1965 and 1970.

Application of equations 9 and 10 between 1965 and 2006, results in the north-west drift of the SAA for the past 40 years, as shown in Figure 4.

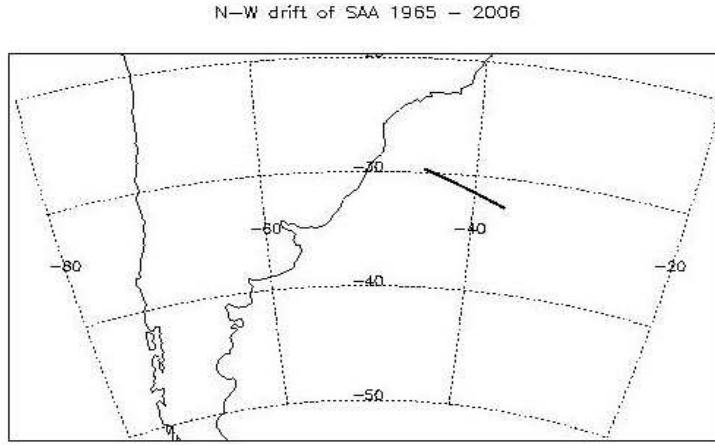


Figure 4. North-westward drift of the SAA between 1965 and 2006.

The proton omni-directional flux spectrum, $f_p(r, \phi, \theta, E, t)$, at any location and time is then extrapolated¹² using the following functional form

$$f_p(r, \phi, \theta, E, t) = f_{P,MIN}(r, \phi, \theta, E) * \exp[-a_p(DRNM * F_{10.7})] \quad (11)$$

In equation (11), the quantity $(DRNM * F_{10.7})$ is averaged over the prior 14 months at solar minimum and 2 months at solar maximum as was determined to be the best fit to the limited NOAA PRO model data set³³. Following the NOAA PRO analysis of Huston and Pfitzer³³, we use the proton flux at solar minimum with

$$f_{P,MIN}(r, \phi, \theta, E) = 0.5 f_{AP8MIN}(r, \phi + 4.1 + 0.19\Delta t, \theta - 2.4 - 0.07\Delta t, E) \quad (12)$$

and solar maximum with

$$f_{P,MAX}(r, \phi, \theta, E) = 0.6 f_{AP8MAX}(r, \phi + 8 + 0.19\Delta t, \theta - 4.8 - 0.07\Delta t, E) \quad (13)$$

Note the scale factors of the prior model¹² have decreased after changing the AP8 MIN field model from IGRF(1965) to Jensen and Cain and AP8 MAX field model from US C&GS/1970 model to GSFC 66/12 for 1970.

B. Geomagnetic Transmission Factor

In the past, the commonly used geomagnetic transmission factor was based on the extrapolation of a world map of vertical cutoff rigidities by Smart and Shea³⁴. In this model, it was assumed that there is no transmission below the vertical cutoff, and 100% transmission (excluding the Earth's shadow) above the vertical cutoff, while in fact there is partial transmission, which is dependent on the angle of incidence relative to the east direction.

The composition of GCR is comprised of multiply charged nuclei of the chemical elements that appear with energies having spectral range of many decades. GCR particles at LEO that are modulated by the geomagnetic field carry a large number of ions that interact with Earth's upper atmosphere. Low energy GCR particles are relatively easy to slow down and all particles below a certain threshold energy are blocked by the Earth's geomagnetic field. In contrast, high energy GCR particles, due to their long interaction range, are more difficult to block. In Figure 5, six naturally abundant ions (H, He, C, O, Si, Fe) have been chosen to show their distribution as a function of energy. It can be seen that the GCR spectrum is dominated by the presence of proton and helium ions. Figure 5 (left) represents the free space GCR particle environment. Figure 5 (right) shows the ISS orbiting environment. The key difference between the figures is that the ISS is orbiting inside the Earth's geomagnetic field and in the Earth's shadow, which blocks all particles with energy less than approximately 20 MeV/n. In addition, the geomagnetic field, due to Lorentz interaction with the GCR ions, decreases the amount of effective range of any charged GCR particle traveling through it, which can be seen through direct comparison of the figures. The comparison shows that the relative abundance of most particles is decreased by roughly one order of magnitude, and particles that are lower in energy (less than 100 MeV/n) lose 10 times more energy by passing through the geomagnetic field. Alternately, high-energy particles (greater than 1 GeV/n) are attenuated by a factor of 5. Finally, at the highest energies, the geomagnetic field has limited capabilities in blocking or even slowing these particles at the ISS altitude.

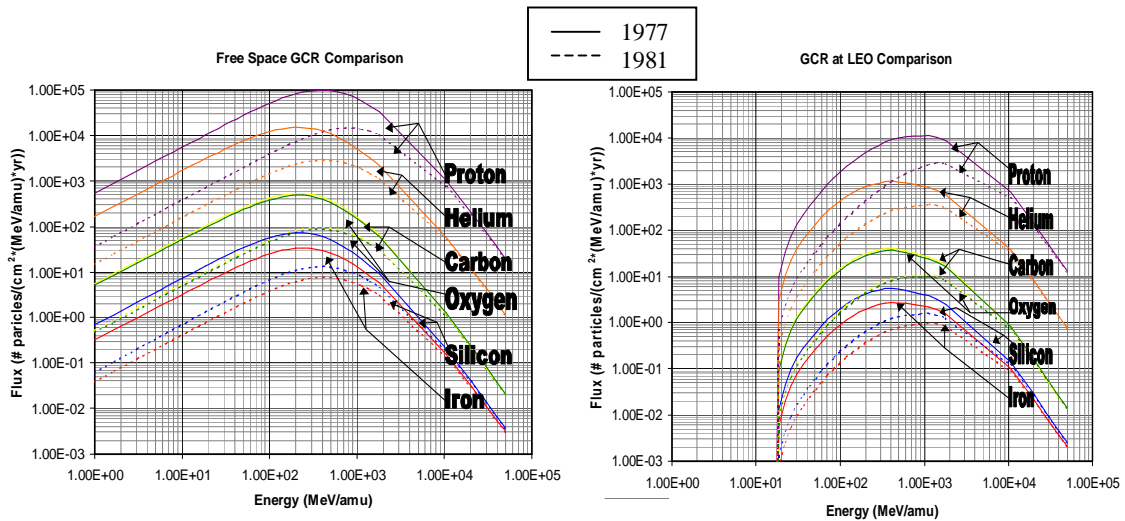


Figure 5. Flux intensities of 6 selected GCR ions in free space and LEO (ISS).

It is most convenient to characterize the geomagnetic interaction of GCR particles in terms of rigidity, R (momentum/unit charge) rather than energy. A common method of representing GCR transmission through the geomagnetic field is the use of a computed local vertical cutoff rigidity, R_{VC} , for which transmission is unity for $R > R_{VC}$ and zero otherwise.

After a lengthy derivation, an expression for the directional distribution of cutoff rigidity was developed by Størmer³⁵, which described the interaction of a charged particle with a dipole magnetic field in terms of the dipole magnetic moment and the directional coordinates. This expression for directional cutoff rigidity, R , in terms of distance from the magnetic dipole center, r_D , and magnetic latitude, λ_M , is usually given by

$$R = \frac{C_D \cos^4 \lambda_M}{r_D^2 \{1 + (1 - \cos^3 \lambda_M \sin \zeta \sin \psi)^{1/2}\}^2} \quad (14)$$

where ζ is the zenith angle, and ψ is the azimuth angle measured clockwise from magnetic north. The constant C_D is directly proportional to the dipole moment, and has a value of 58.0 GV for the 1990 IGRF dipole. The nomenclature used above is essentially that of Cooke³⁶. Equation 14 basically indicates that particles with lower rigidity values are transmitted as incidence angles become more aligned with the geomagnetic field. For this reason, higher GCR flux values for low rigidity particles can access the polar regions in near vertical directions, whereas at low and mid latitudes, a distinct cutoff rigidity appears for which no particles are transmitted. For this simplified model, the rigidity for vertically incident particles is

$$R_{VC} = C_D \cos^4 \lambda_M / 4r_D^2 \quad (15)$$

This simple dipole approximation may be improved upon by utilizing detailed calculations of vertical cutoff rigidity evaluated from the multipole field models. Global maps of cutoff rigidity have recently become available³⁷, and have been incorporated in the present work. The temporal variation of the GCR flux is also taken from the detailed vertical cutoff calculations of reference 37 for time intervals covering most of the last half century and reflecting the varying field strength observed during this period. In the present model, we use the IGRF field model evaluated for arbitrary dates from 1945 to 2020. Typical cutoff rigidities of the model at two locations over the Earth in 2006 are shown in Figure 6.

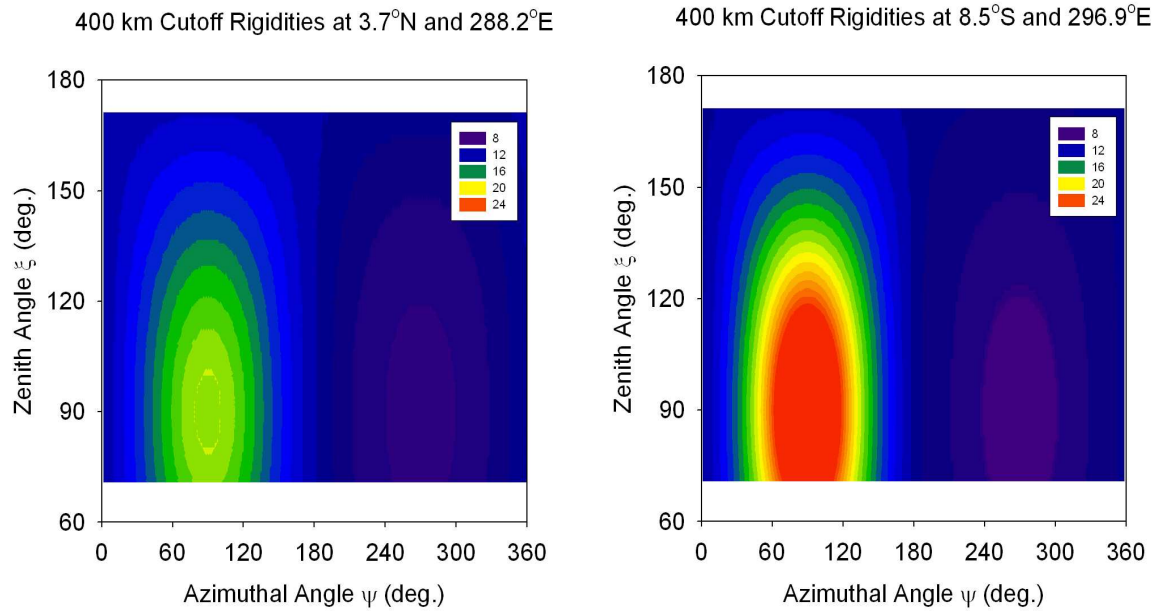


Figure 6. 2006 geomagnetic cutoff rigidities at 400 km at 3.7°N-288.2° E (left) and 8.5°S-296.9°E (right).

III. Description of Computational Procedure

The current environmental code used to model the trapped proton and GCR environments consists of two routines. The main program, GEORAD, controls the input/output and computational grid definition and following subroutine, RADAVE, performs Spacecraft to Local Vertical (SC-LV) coordinate conversion and controls GCR and proton flux calculations. The program requires several large database files: AP8MIN and AP8MAX proton flux files, global vertical cutoff data (15 sets for years between 1945 and 2000), and spherical harmonic expansion coefficients for IGRF fields between 1945 and 2005. Several smaller database files are also required: the Deep River Neutron Monitor (DRNM) count rate records, F10.7 radio frequency flux data, and two special sets of magnetic field coefficients for AP8 flux evaluations. In addition, GEORAD requires a user-supplied trajectory file for orbital position definition, which is comprised of a series of values for time, latitude, longitude, altitude, yaw, pitch, and roll.

The calculations performed during execution are controlled by a series of option flags. Initiating execution leads first to the definition of energy and rigidity grids and a directional grid of azimuth and polar angles. The directional grid, as depicted in Figure 7, consists of 970 rays subtending equal solid angles defined by 44 equally spaced azimuth angles and 22 polar angles, plus 2 polar rays.

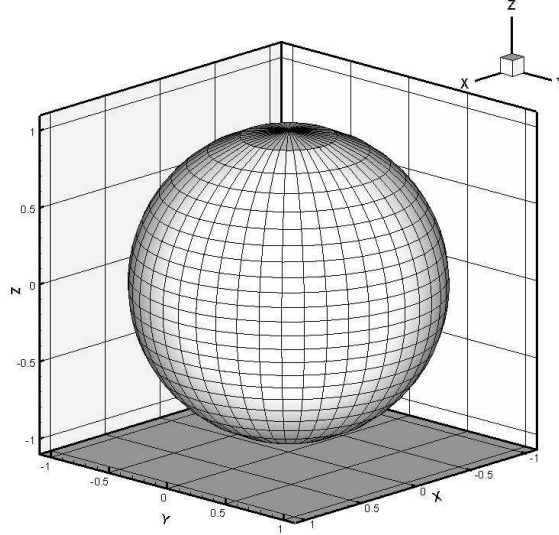


Figure 7. Directional grid (sphere) with 970 rays.

Each element of the surface solid angle complies with the following requirements to assure even distribution of directionality. We define each solid angle element by:

$$\Delta\Omega = \Delta\phi \int_{\cos\theta_{i-1}}^{\cos\theta_i} d(\cos\theta) = \Delta\phi(\cos\theta_i - \cos\theta_{i-1}) \quad (16)$$

or

$$\cos\theta_i = \frac{\Delta\Omega}{\Delta\phi} + \cos\theta_{i-1} \quad (17)$$

Using definitions $\Delta\Omega = \frac{4\pi}{N}$, $\Delta\phi = \frac{2\pi}{N_\phi}$, and $N = N_\phi \cdot N_\theta$, where $N_\phi = 44$ and $N_\theta = 22$, results

in

$$\frac{\Delta\Omega}{\Delta\phi} = \frac{4\pi / N}{2\pi / N_\phi} = \frac{2N_\phi}{N} \quad (18)$$

Combining equations 17, and 18 yields

$$\cos \theta_i = \frac{2N_\phi}{N} + \cos \theta_{i-1} \quad (19)$$

providing an iterative process to calculate all 22 zenith values.

Once the rays are defined, the spacecraft (SC) coordinate system is mapped into a local vertical (LV) coordinate system where magnetic field quantities are calculated . Figure 8 depicts the relationship between the two coordinate systems.

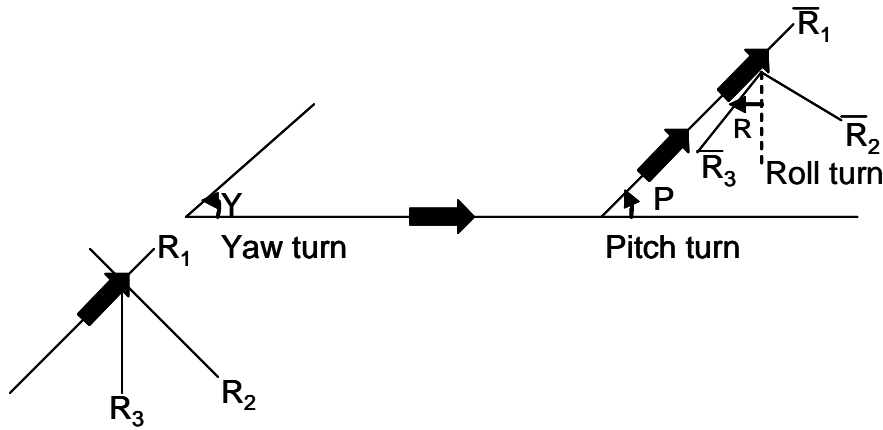


Figure 8. Graphical relationship between SC and LV coordinate systems.

Here, the rotational mapping complies with the following matrix relationships

$$R_{SC}(R) = \begin{bmatrix} 1 & 0 & 0 \\ 0 & \cos R & -\sin R \\ 0 & \sin R & \cos R \end{bmatrix} \quad (20a)$$

$$R_{SC}(P) = \begin{bmatrix} \cos P & 0 & \sin P \\ 0 & 1 & 0 \\ -\sin P & 0 & \cos P \end{bmatrix} \quad (20b)$$

$$R_{SC}(Y) = \begin{bmatrix} \cos Y & -\sin Y & 0 \\ \sin Y & \cos Y & 0 \\ 0 & 0 & 1 \end{bmatrix} \quad (20c)$$

Implementation of equation 20 matrices result in the following relation between the SC and LV coordinate systems

$$R_{SC}(Y, P, R) = R_{SC}(Y)R_{SC}(P)R_{SC}(R)R_{LV}(Y, P, R) \quad (21)$$

with the inverse transform being

$$R_{LV}(Y, P, R) = R_{SC}^{-1}(R)R_{SC}^{-1}(P)R_{SC}^{-1}(Y)R_{SC}(Y, P, R) \quad (22a)$$

or in expanded form as

$$R_{LV}(Y, P, R) = \begin{bmatrix} 1 & 0 & 0 \\ 0 & \cos R & \sin R \\ 0 & -\sin R & \cos R \end{bmatrix} \begin{bmatrix} \cos P & 0 & -\sin P \\ 0 & 1 & 0 \\ \sin P & 0 & \cos P \end{bmatrix} \begin{bmatrix} \cos Y & \sin Y & 0 \\ -\sin Y & \cos Y & 0 \\ 0 & 0 & 1 \end{bmatrix} R_{SC}(Y, P, R) \quad (22b)$$

which for the desirable coordinate system $R_{LV}(Y, P, R)$ results in

$$R_{LV}(Y, P, R) = \begin{bmatrix} \cos P \cos Y & \cos P \sin Y & -\sin P \\ -\sin Y \cos R + \sin R \sin P \cos Y & \cos R \cos Y + \sin R \sin P \sin Y & \sin R \cos P \\ \sin R \sin Y + \cos R \sin P \cos Y & -\cos Y \sin R + \cos R \sin P \sin Y & \cos R \cos P \end{bmatrix} R_{SC}(Y, P, R) \quad (23)$$

GCR calculations are performed by accessing the vertical cutoff database and interpolating for the appropriate time, latitude, and longitude. The angular distribution of rigidities is calculated and converted to 0 or 1 transmission over the range of directional grid values. The cumulative directional transmissions are available for direct output or they can be averaged to obtain an “effective” GCR transmission.

The proton flux calculation begins by calculating the standard AP8MIN and AP8MAX omnidirectional flux for the specified time and global position. Solar cycle modulation is then applied to obtain a final proton omni-flux spectrum. The direction distribution function is applied to the final omni-flux spectrum to provide a vectorial proton flux. The cumulative directional flux or the averaged omni-flux are both available for direct output. Figure 9 presents a computational flow diagram for GEORAD.

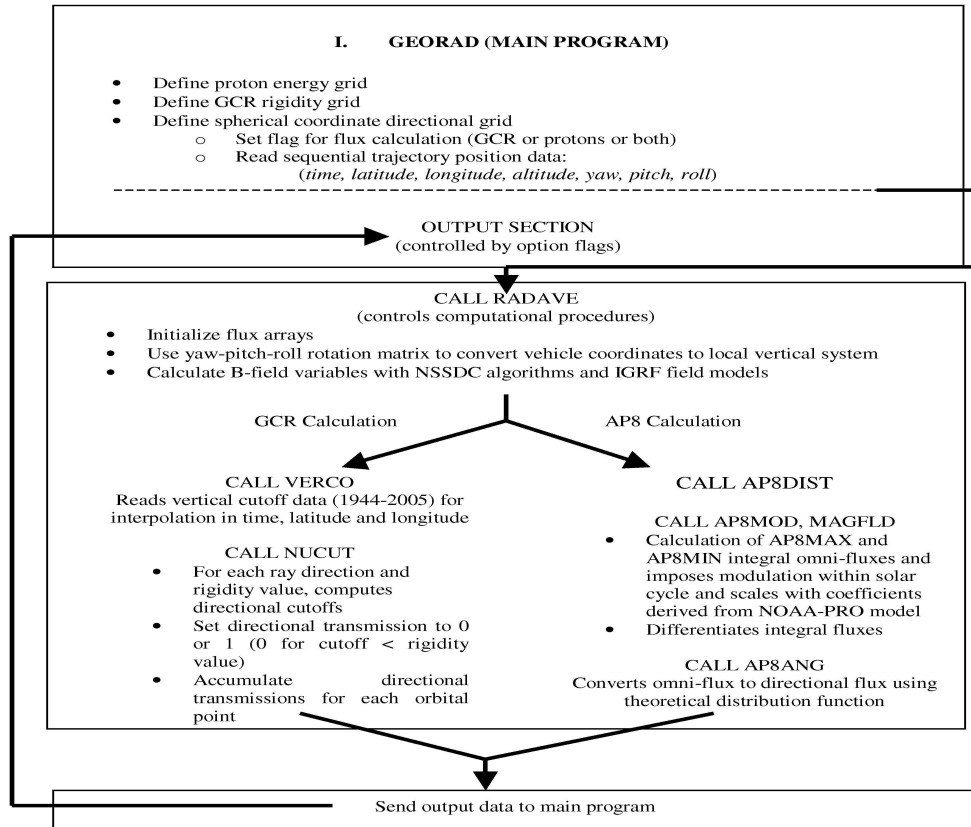


Figure 9. Schematic diagram of computation flow for GEORAD.

IV. Demonstration of Anisotropic Environment

Unlike STS, which is a highly maneuverable craft and thus the omni-directional environmental model is sufficiently applicable to describe its environment, ISS is normally stabilized in the local vertical reference frame; hence, the direction of arrival of environmental particles plays an important role in describing its environment. This directionality of arriving protons is especially important if shield augmentation of the habitable volume is considered.

In this work, the ISS idealized circular orbit is selected for analysis, with the goal of a somewhat detailed examination of the directional aspects of the cumulative trapped protons and GCR. Since the ISS orbit is in LEO, the single orbit considered is tailored to pass through the center of the SAA, presently (2006) centered near 29.7°S, 315.2°E. The global tracks of this orbit is shown in Figure 10.

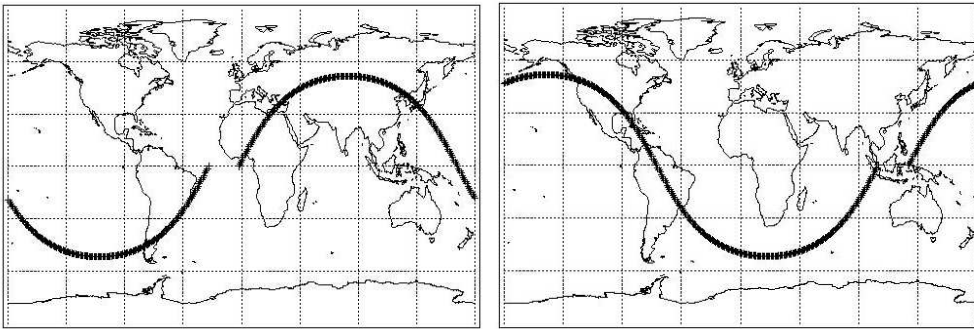


Figure 10. Single ISS ascending (left), and descending (right) orbit tracks (400 km., 51.6°) crossing 2006 SAA center.

The ISS chosen orbit is intended to represent typical conditions for human operations in LEO. Calculated results are performed for ISS orientation with zero pitch and roll angles, with yaw angle prescribed by the horizontal heading with respect to the geographic north.

A. Results for Trapped Proton Vector Flux

The trapped protons exhibit more pronounced directional characteristics than the GCR primarily because of the different nature of the source of radiation, and the inherently lower energy range of the trapped particles. For the typical LEO orbit, the proton flux of interest is of importance only in the SAA vicinity. This is also a region of particle path reversal (“mirror point”) where the pitch angle approaches and recedes from its 90° limiting value. Thus, proton flux is expected to be confined to pitch angles nearly perpendicular to the local B field vector, which in this region results in a high intensity flux band tilted normally to the magnetic dip angle. The directional differential proton flux is calculated for all proton energies specified in the grid of values in the range of 0.1 - 500 MeV. A number of diagnostic calculations have shown that directional distributions are relatively insensitive to energy value, especially for the

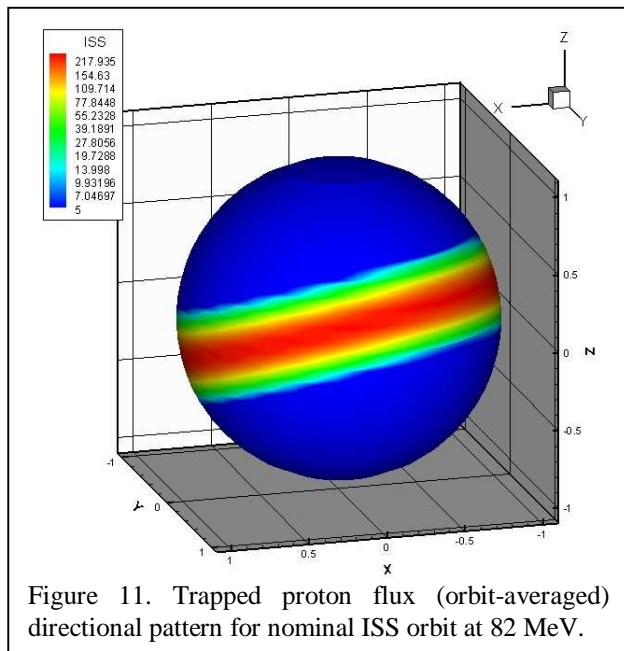


Figure 11. Trapped proton flux (orbit-averaged) directional pattern for nominal ISS orbit at 82 MeV.

higher energies of most interest ($> \sim 50$ MeV) for a pressurized spacecraft. In order to demonstrate the directional results, a single grid point energy value (82 MeV) has been selected for graphical display. In the case of the nominal ISS orbit, the expected band of high proton flux is especially prominent, as shown in Figure 11. These results represent the orbit averaged directional flux. However, since flux contributions appear only in the relatively short trek across the SAA (~ 10 minutes duration), the directional flux pattern is established for a relatively narrow range of magnetic dip angles.

When the directional flux is integrated over the total 4π solid angle, an omni-directional flux is obtained, as is shown in Figure 12. The discrepancy between ascending and descending nodes at lower energies can be accounted for by the presence of extremely low energy particles (< 10 MeV at 400 km) in the deep southern latitudes due to the “southern proton aurora region”, through which, for the chosen two treks through the SAA, only the descending node of ISS passes. From a dosimetric point of view, these low energy protons essentially have no contribution to the radiation within the interior of the spacecraft.

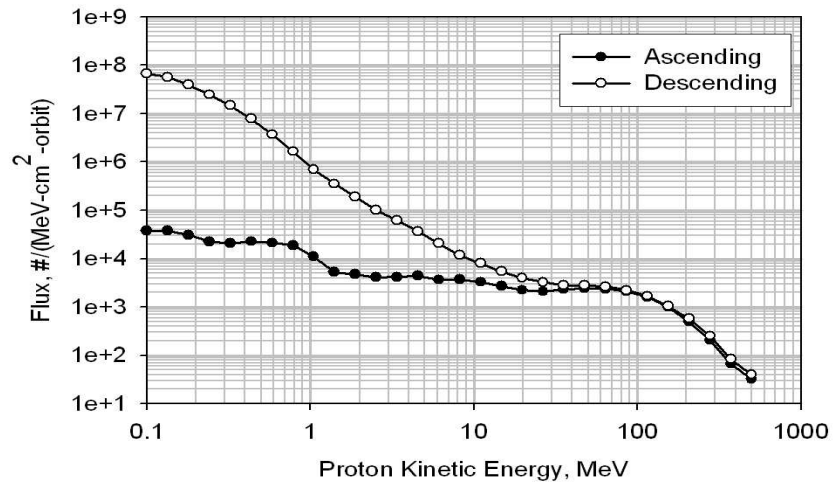


Figure 12. ISS orbit accumulated omni-directional differential proton flux for a single pass through SAA.

For ISS trajectory (400 km., 51.6°), the contributions of the “southern proton aurora region” to AP8 models are shown on a world map in Figure 13. Note that only during the descending orbit through the SAA does the ISS encounter this region of low energy particles.

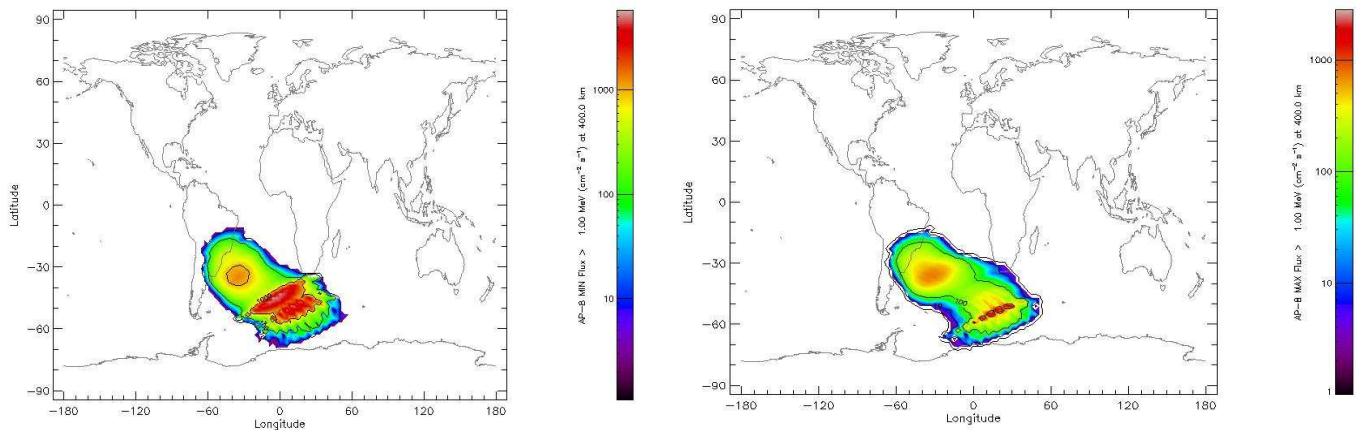


Figure 13. Contribution of low energy aurora protons, courtesy of SPENVIS <http://www.spenvis.oma.be/>

The omni-flux environment can be applied directly to a randomly oriented spacecraft. For long duration missions in LEO involving many orbital transits, it is found that exposure rates for GCR and trapped protons in moderately shielded spacecraft (e.g., STS, ISS) are of similar magnitudes³⁸. In the case of spacecraft orbiting in approximately fixed orientation (e.g., ISS), the directional exposures for GCR are relevant over the entire field of view, while the trapped protons exhibit much more pronounced directionality that imply consideration of special shield design strategies.

In this work, the selected ISS track over the SAA region is chosen in such a manner that minute by minute trajectories in ascending and descending nodes provide sufficient information to calculate the proton flux in 2006 based on NOAA PRO modulations of AP8 MIN (1965) and AP8 MAX (1970) epochs. Figure 14 depicts the ascent and descent orbital tracks with overlaid integral proton flux contours ($E > 100$ MeV) based on the AP8 MIN and the AP8 MAX.

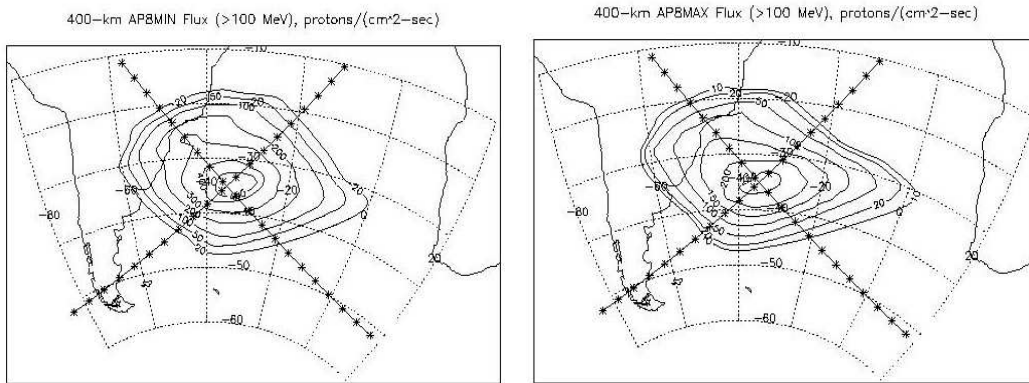


Figure 14. Ascent and descent orbital tracks of ISS through the SAA for AP8 MIN, and AP8 MAX. Spacing (*) represents 1 min. intervals.

Using the proton environmental model and minute by minute trajectories of Figure 14, the omni-directional proton differential spectra were then calculated, and for selected points near the region of peak flux (i.e. SAA), are depicted in Figure 15. The chosen points are identified by time values in minutes elapsed after ascending and descending node points.

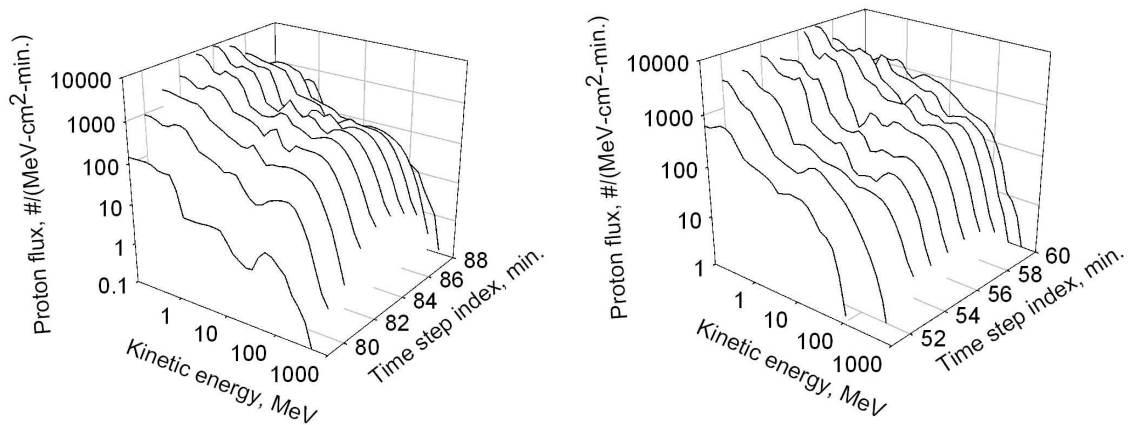


Figure 15. Omni-directional differential proton flux obtained from the trapped proton model in central region of the SAA for ascending (left) and descending tracks (right).

The complex (erratic) low energy behavior ($\sim < 10$ MeV) in the proton spectra can not be readily explained, and is most likely due to several contributing factors, including the usage of simple numerical interpolation. However, since only higher energy protons ($> \sim 50$ MeV) penetrate the ISS structure, the low energy fluctuations are not of much practical importance.

B. Results for GCR Transmission

In order to demonstrate salient features of directionality of GCR cutoff rigidity, two time points have been chosen for the case of the nominal ISS orbit. At the orbital position occurring near 30° N, the cutoff rigidity does not vary dramatically for the portion of the directional sphere above the earth shadow. Figure 16, (left), shows the directional pattern associated with the cutoff rigidity at this location in the orbit. Even though the range of rigidity values is not large, the expected east-west asymmetry is clearly seen. In Figure 16, (right), a similar “snapshot” of the directional rigidity is shown at an equatorial location. Here, the directionality is much more pronounced, and the range of calculated values is much larger. Each figure shows a darkened region for inaccessible directions due to the effect of earth shadowing.

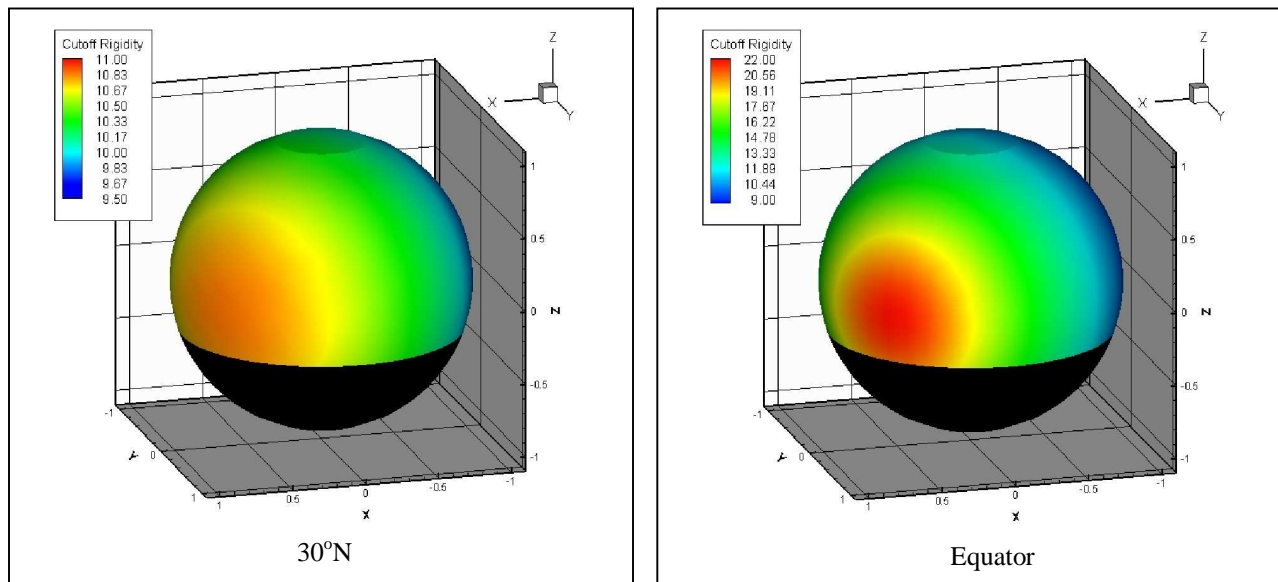


Figure 16. Pattern of directional cutoff rigidity for nominal ISS orbit at 30° N (left), and equator (right).

Calculations for which the rigidity values are averaged over all orbital time steps exhibit much more uniformity over the directional sphere since the vehicle heading angle undergoes large changes in the course of this relatively high inclination orbit. Directional calculations should prove particularly useful in validation studies involving active particle flux monitors, and dosimeters for which directional response is well defined.

From the standpoint of total mission exposures, the cumulative GCR transmission averaged over all directions becomes significant since it may be related directly to incurred dose by means of standard environment models of GCR flux spectra. An example is the ISS mission averaged transmission coefficient ($0 < T < 0.8$) as a function of rigidity, as shown in Figure 17. Note that the figure compares the vertical cutoff rigidity versus cutoff rigidity where directionality is averaged over the entire sphere. The figure indicates that at R values in the range of 10 – 20 GV, the vertical cut off model allows more particles to penetrate the field than the cutoff rigidities that are directionally averaged.

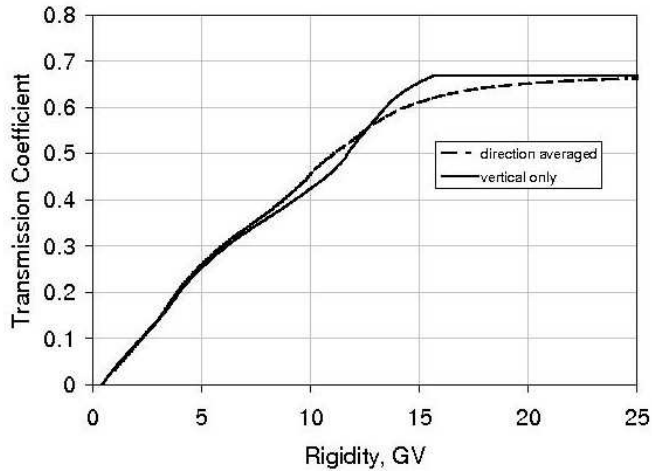


Figure 17. ISS transmission coefficients for vertical cut off rigidity and direction averaged rigidity.

V. Impact on ISS Shielding

A. Correlation with STS TLD Data

In an attempt to validate the model we combined the omni-directional trapped proton model with the Badhwar-O'Neill GCR model³⁹ using vertical cutoff geomagnetic transmission factors (not dependent on angle) and a neutron albedo model¹², and compared with 17 years of Shuttle TLD data. The points of comparison were chosen at random over the 17 years covering nearly two solar cycles and a broad range of altitudes³¹ as shown in Table 2. It is seen that all points are within 15% of TLD measurements.

Flight	Date	DRNM*	DLOC	TLD† (μGy/d)	Calc. (μGy/d)
STS-41A	11/83	6421	3	64.6	59.6
STS-51D	4/85	6661	4	917.4	889.3
STS-31	4/90	5701	1	2141	2290
STS-43	8/91	5894	4	20.7	18.6
STS-62	3/94	6771	1	94.3	89.2
STS-65	7/94	6822	2	28.3	25.1
STS-67	3/95	6925	3	250.8	238.1
STS-80	11/96	6973	4	264.4	256.5
STS-82	2/97	7074	1	2978	3080
STS-91	6/98	6894	1	89.1	83.2
STS-101	5/00	6460	2	140.8	131.1
STS-92	10/00	6417	2	165.9	153.4

Table 2. Comparison of present model with Shuttle flight data (* Deep River Neutron Monitor count rate, † GCR corrected TLD100 data).

B. Energetic Proton Transport in Shield Medium

The proton spectra of Figure 15 along with GCR spectra of reference 39 were used as input to the HZETRN code to compute transport through thickness ranges of shield material (Al). Subsequent exposures in simulated tissue (H₂O) are evaluated as dose equivalents using ICRP-60⁴⁰ quality factors for normally incident flux on semi infinite slab geometry. The NASA Langley HZETRN code is a well established deterministic procedure allowing rapid and accurate solution to the Boltzmann transport equation. Details concerning the interaction and attenuation methodology are described at length elsewhere¹³. Figure 18 shows the resultant total dose equivalent vs. depth functions obtained from the

transport calculations through the aluminum slab, and are used to evaluate ultimate exposures at target points within complex shield configurations defined by the desired CAD solid model of the full scale geometric structure (e.g. ISS).

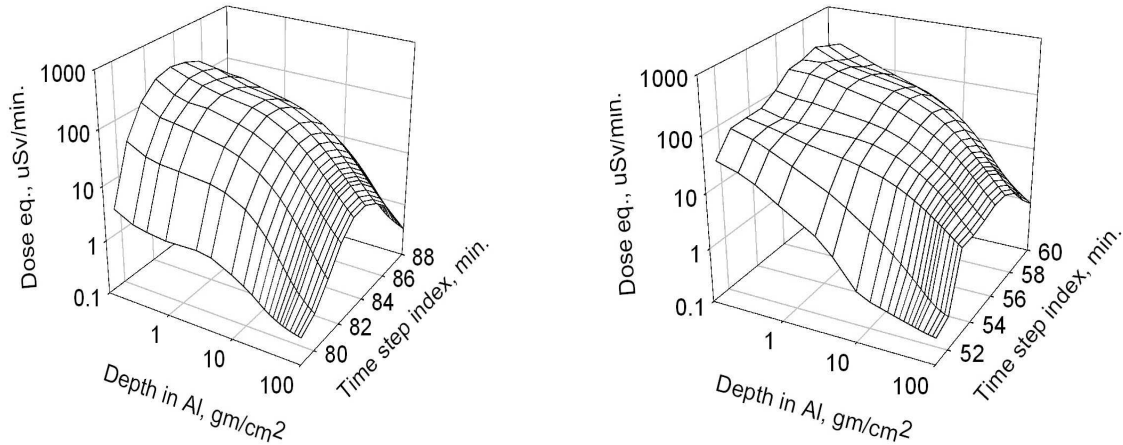


Figure 18. Total dose equivalent vs. depth functions calculated for Aluminum slab geometry at selected times during the SAA transit: ascending tracks (left); and descending tracks (right).

C. Comparison with TLD Measurements from ISS 6A and ISS 7A

Descriptions of the 6A and 7A configurations can be found in Hugger et al⁴¹. The accumulated TLD100 values at 11 target points have been calculated for the respective ISS trajectories using both omni and directional environmental models. Five of the selected target points are located in the U.S. Lab Module and six are distributed throughout the Russian Service Module. Figures 19 through 22 display the results of these calculations compared with the TLD measurements from ISS 6A and ISS 7A.

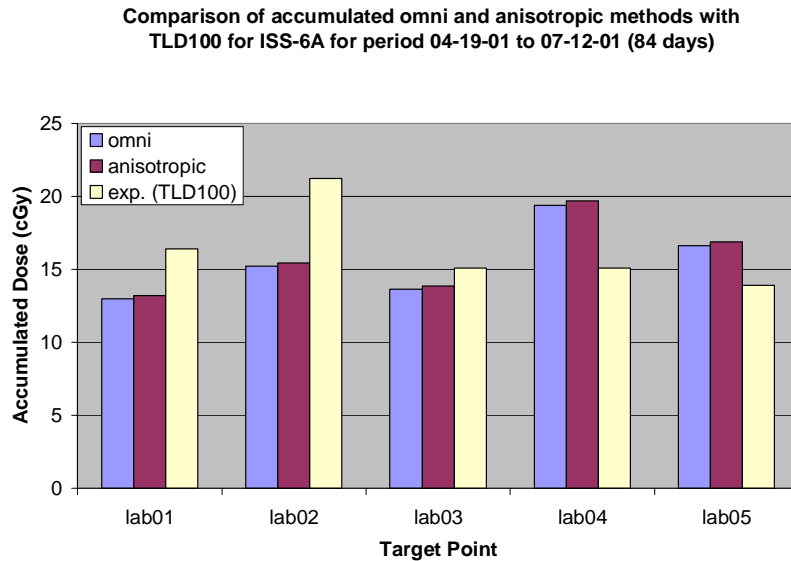


Figure 19. Comparison of accumulated TLD100 predicted by omni and directional environmental models with ISS 6A TLD measurements for target points located in the U.S. Lab Module.

Comparison of accumulated omni and anisotropic methods with TLD100 for ISS-6A for period 04-19-01 to 07-12-01 (84 days)

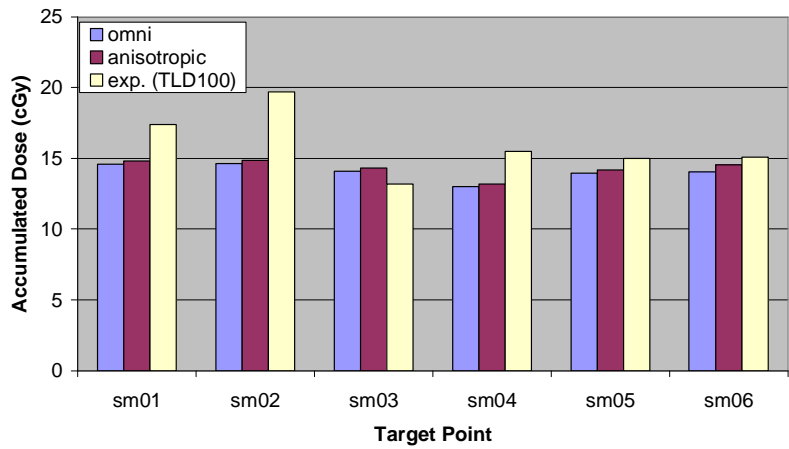


Figure 20. Comparison of accumulated TLD100 predicted by omni and directional environmental models with ISS 6A TLD measurements for target points located in the Russian Service Module.

Comparison of accumulated omni and anisotropic methods with TLD100 for ISS-7A for period 07-12-01 to 08-22-01 (40 days)

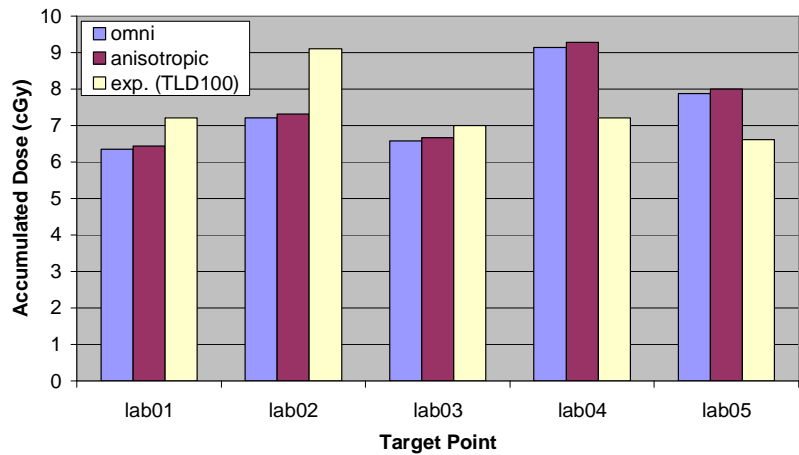


Figure 21. Comparison of accumulated TLD100 predicted by omni and directional environmental models with ISS 7A TLD measurements for target points located in the U.S. Lab Module.

Comparison of accumulated omni and anisotropic methods with TLD100 for ISS-7A for period 07-12-01 to 08-22-01 (40 days)

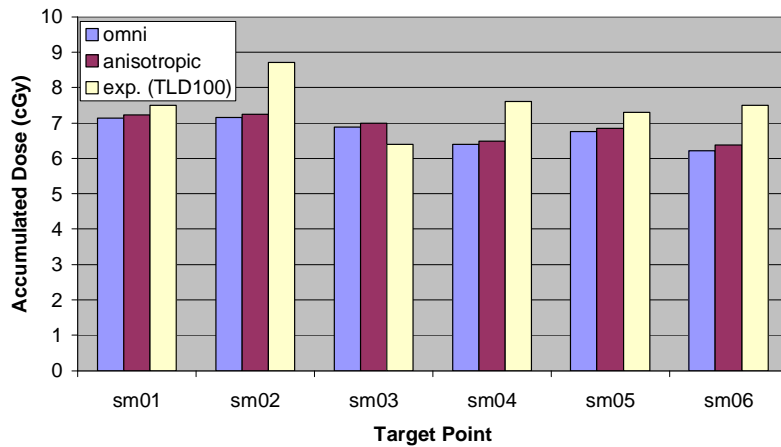


Figure 22. Comparison of accumulated TLD100 predicted by omni and directional environmental models with ISS 7A TLD measurements for target points located in the Russian Service Module.

These bar charts show that the values calculated using the anisotropic model for the service module target points correlate well with the experimental TLD100 measurements and in most cases predict more accurate values than the omni method. The directional values predicted for the lab target points are also more accurate than those predicted by the omni method. These results give us reason to believe that the incorporation of directionality into the LEO environmental model has indeed improved their ability to predict the appropriate dosimetric responses within ISS.

D. Analysis using CAD Solid Model of ISS 11A Configuration

We will now apply the directional environmental models for LEO to the current configuration of ISS. The primary components of the ISS 11A configuration are the U.S. Destiny Lab Module, the U.S. Unity Connection Module (Node 1), the U.S. Airlock, and the three U.S. Pressurized mating Adaptors (PMA's). Other components include the Russian Functional Cargo Block (FGB, or Zarya), the Russian Service Module, the Russian Soyuz Spacecraft, the Russian Progress resupply vehicle, the Russian Docking Compartment, and truss structures. A simplified model of this configuration has been constructed for shield analysis using the commercially available CAD software I-DEAS. The model consists of 460 separate components, each with individual dimensions, orientation, and density distribution. Shielding for the interior is primarily from the distributed micrometeoroid shield and the pressure vessel. Additional shielding occurs from the cargo in the primary modules.

Six target points within ISS 11A have been selected for evaluation. Figures 23 through 25 show the external view of the 11A CAD model and the locations of the six target points.

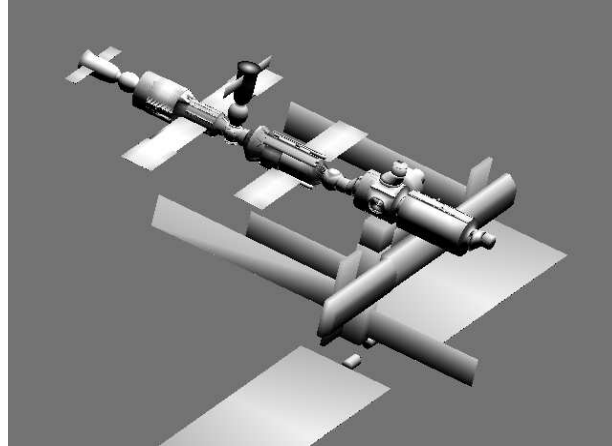


Figure 23. External view of CAD Modeled ISS 11A configuration.

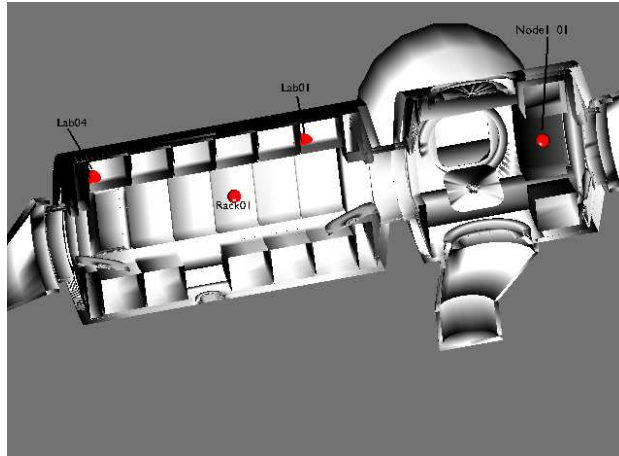


Figure 24. Split view of U.S. Lab Module showing selected target points.

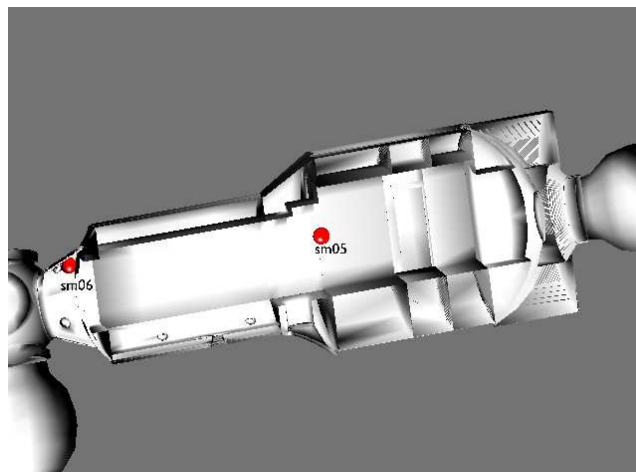


Figure 25. Split view of Russian Service Module showing selected target points.

The thickness distributions of the 970 rays have been evaluated in terms of the scaled thickness in g/cm^2 for each of the six selected target points. Figure 26 gives the cumulative thickness distributions for the six points.

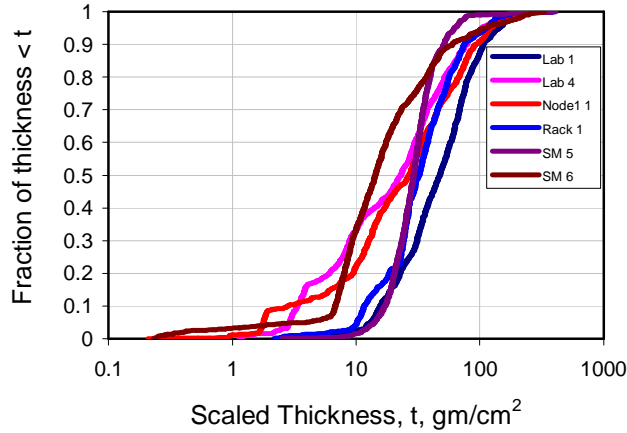


Figure 26. Cumulative thickness distribution for selected target points in ISS 11A configuration.

Table 3, provides the predicted dose equivalent rates at each of the six target points for ascending and descending trajectories using both the omni and directional environmental models. Each entry represents the solid angle integration of dose equivalent rate resulting from protons incident on the target point from all directions. TLD100 rate predictions (not shown) have also been calculated and are ready for experimental comparison.

ASCENDING TRACK												
RACK01		LAB1		LAB4		NODE1_1		SM5		SM6		
TS	Directional	Omni	Directional	Omni	Directional	Omni	Directional	Omni	Directional	Omni	Directional	Omni
79	0.55	0.69	0.44	0.56	1	1.13	0.85	0.97	0.51	0.67	1.24	0.35
80	3.72	3.95	2.52	2.74	8.44	8.57	7.2	7.34	3.38	3.62	10.36	10.5
81	11.37	11.5	7.84	8.05	24.32	24.2	21.36	21.3	10.79	11	29.42	29.3
82	22.31	21.6	16.03	15.5	44.25	43.2	39.99	39	21.49	20.8	52.35	51.2
83	32.45	31.3	23.98	23	60.92	59.3	52.89	51.4	31.8	30.6	74.74	72.9
84	32.54	31.3	24.21	23.2	59.47	57.9	51.78	50.3	32.14	30.9	73.74	72
85	23.95	23.1	17.75	17	43.97	42.8	38.1	37	23.67	22.8	55.17	53.8
86	14.48	14	10.61	10.2	27.39	26.7	24.29	23.7	14.18	13.7	33.77	33
87	6.06	5.9	4.36	4.23	12.25	12	11.07	10.8	5.86	5.69	15.18	15
88	1.06	1.31	0.77	0.99	2.25	2.48	2.04	2.26	0.99	1.28	3.35	3.58

DESCENDING TRACK												
RACK01		LAB1		LAB4		NODE1_1		SM5		SM6		
TS	Directional	Omni	Directional	Omni	Directional	Omni	Directional	Omni	Directional	Omni	Directional	Omni
51	0.42	0.55	0.35	0.46	1.28	1.41	1.26	1.38	0.36	0.5	2.47	2.6
52	2.18	2.2	1.53	1.57	5.54	5.51	5.19	5.17	2	2.02	9.69	9.59
53	15.46	14.4	12.26	11.3	22.97	21.8	20.86	19.7	15.94	14.8	29.51	28.2
54	21.26	20.1	16.21	15.2	32.87	31.6	29.22	28	21.97	20.7	42.07	40.6
55	23.91	22.7	18.13	17.1	39.15	37.8	34.95	33.6	24.39	23.1	47.53	46
56	30.68	29.4	22.92	21.8	54.09	52.5	48.37	46.8	30.8	29.4	69.81	67.9
57	32.69	31.6	24.02	23.1	60.45	58.9	52.77	51.3	32.32	31.2	75.8	74
58	24.77	24.1	17.86	17.3	48.86	47.8	43.06	42.1	23.85	23.1	49.46	58.2
59	12.4	14.1	8.2	9.88	29.95	31.2	26.26	27.6	11.34	13.2	34.06	33.3
60	4.26	5.59	2.72	3.9	14.33	15.4	12.49	13.6	3.26	4.75	17.26	18.3

Table 3. Minute by minute dose equivalent rate (uSv/min) for six selected target points within ISS 11A, for isotropic and directional proton environments within the SAA (TS indicates time step).

Table 3 indicates that the proton dose rates are of similar magnitude for both omni and directional external environments. Results from ISS 6A and 7A also indicated that we should expect about a 5% improvement in the values predicted using a directional environment.

Even though the total doses are of the same magnitude for both isotropic and vectorial external environments, the directional properties of the radiation field may be vastly different for the two cases. This is illustrated in Figure 27 for the target point designated RACK01 as contour plots of the directional dose equivalent. The directionality of the incurred dose has possible design implications for optimal shielding design.

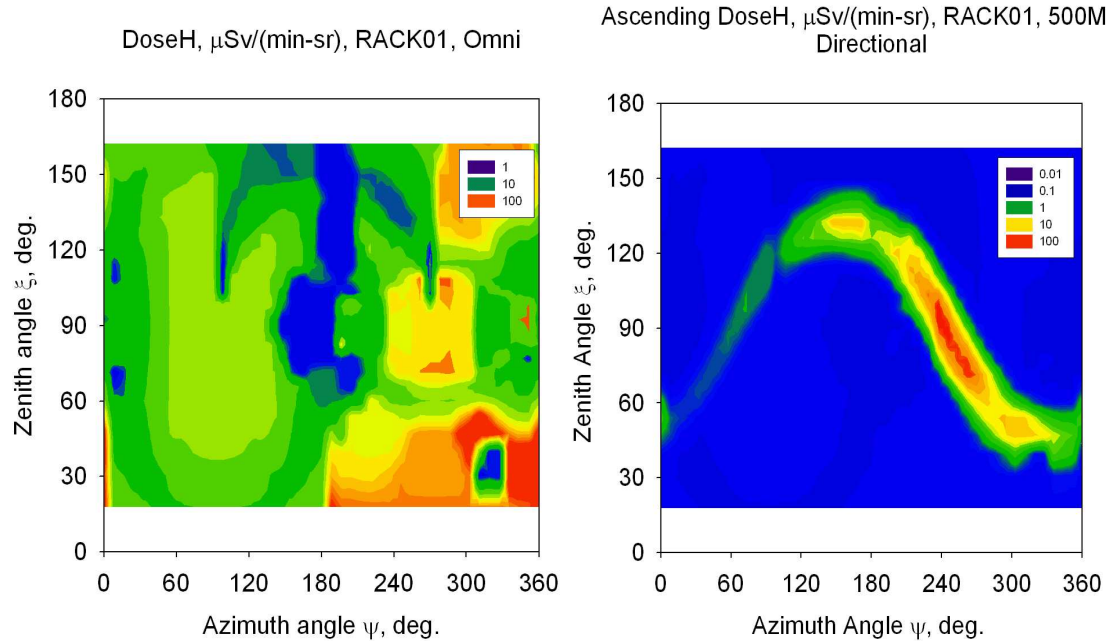


Figure 27. Contour plots of directional dose equivalent at target point RACK01.

VI. Concluding Remarks

The use of physics-based scaling of the trapped radiation environment has proven remarkably accurate considering the simplicity of the procedure. The addition of the angular dependence further increases the usefulness of the basic models. Such developments are of importance due to the increased human activity in LEO and a necessary development for further infrastructure deployment in Earth's neighborhood.

The CEV concept is envisioned as the next piloted interplanetary spacecraft. Even early preliminary designs will require considerable configuration details as well as definition of likely mission scenarios and timelines. It is important that radiation exposure analysis is incorporated into the early design phases for several reasons. If the CEV is temporarily stationed at ISS, it would spend most of that time in a fixed orientation, for which knowledge of the directional flux environment is a factor. The escape trajectory definition is important since passage through the high intensity belt regions may be involved. Radiation protection "fixes" in later stages of the design process are likely to have adverse affects on both budgetary and schedule constraints. It is felt that the present environmental model will be especially useful as a tool that can be advantageously and efficiently implemented in the earliest CEV design phases.

References

1. F. A. Cucinotta et al., Space Radiation and Cataracts in Astronauts, *Radiat. Res.*, no. 156, pp. 460-466, 2001.
2. H. Wu et al., Estimate of Space Radiation-Induced Cancer Risks for International Space Station Orbits, *NASA TM-104818*, 1996.
3. J. W. Wilson, L. W. Townsend, H. Farhat, Cosmic-Ray Neutron Albedo Dose in Low-Earth Orbits, *Health Phys.*, no. 57, pp. 665-668, 1989.
4. V. E. Dudkin et al., Neutron Fluences and Energy Spectra in the Cosmos-2044 Biosatellite Orbit, *Nucl. Tracks Radiat. Meas.*, no. 20, pp. 139-141, 1992.
5. J. E. Keith, G. D. Badhwar, D. J. Lindstrom, Neutron Spectrum and Dose-Equivalent in Shuttle Flights During Solar Maximum, *Nucl. Tracks Radiat. Meas.*, no. 20, pp. 41-47, 1992.
6. G. D. Badhwar et al., A study of the Radiation Environment on Board the Space Shuttle Flight STS-57, *Radiat. Meas.*, no. 24, pp. 283-289, 1995.
7. V. E. Dudkin et al., Studying Radiation Environment on Board STS-55 and STS-57 by the Method of Passive Detectors, *Radiat. Meas.*, no. 25, pp. 483-484, 1995.
8. G. D. Badhwar et al., Measurements of Secondary Particle Energy Spectrum in the Space Shuttle, *Radiat. Meas.*, no. 24, pp. 129-138, 1995.
9. J. L. Shinn et al., Effects of Target Fragmentation on Evaluation of LET Spectra from Space Radiations in Low Earth Orbit (LEO) Environment—Impact on SEU Predictions, *IEEE Trans. Nucl. Sci.*, no. 42, pp. 2017-2025, 1995.
10. J. L. Shinn et al., Validation of a Comprehensive Space Radiation Transport Code, *IEEE Trans. Nucl. Sci.*, no. 45, pp. 2711-2719, 1998.
11. G. D. Badhwar et al., Space Radiation Absorbed Dose Distribution in a Human Phantom, *Radiat. Res.*, no. 157, pp. 76-91, 2002.
12. J. W. Wilson et al., Natural and Induced Environment in Low Earth Orbit, *NASA TM-2002-211668*, 2002.
13. J. W. Wilson et al., HZETRN: Description of a Free-Space Ion and Nucleon Transport and Shielding Computer Program, *NASA TP-3495*, May 1995.
14. J. I. Vette, The NASA/National Space Science Data Center Trapped Radiation Environmental Model Program (1964-1991), *NSSDC/WDC-A-R&S 91-29*, 1991.
15. P. D. McCormack, Radiation Dose and Shielding for the Space Station. *Acta Astronaut.*, no.17, pp. 231-241, 1988.
16. D. C. Jensen, J. C. Cain, An Interim Geomagnetic Field, *J. Geophys. Res.*, no. 67, pp. 3568-3569, 1962.
17. D. M. Sawyer, J. I. Vette, AP-8 Trapped Proton Environments for Solar Maximum and Solar Minimum, *NSSDC/WDC-A-R&S 76-06*, 1976.
18. J.C. Cain et al., A proposed Model for the International Geomagnetic Reference Field-1965, *J. Geomag. Geoelec.*, no. 19, pp. 335-355, 1967.
19. G. D. Badhwar et al., In-Flight Radiation Measurements on STS-60, *Radiat. Meas.*, no. 26, pp. 17-34, 1996.
20. W. Atwell et al., Space Radiation Shielding Analysis and Dosimetry for the Space Shuttle Program, In *High-Energy Radiation Background in Space*, Eds. A. C. Rester & J. I. Trombka, AIP Conference Proceedings, New York, no. 186, pp. 289-296, 1989.
21. W. Atwell, A Summary of the Southern Atlantic Anomaly (SAA) Drift Motion and Trapped Proton Enhancements in the SAA, 34th COSPAR, Houston, TX., October 2002.
22. G. D. Badhwar, Drift Rate of the Southern Atlantic Anomaly, *J. of Geophysical Research*, Vol. 102, no. A2, pp. 2343-2349, Feb. 1997.
23. G. D. Badhwar, V. A. Shurshakov, V. Tsetlin, Solar Modulation of the Dose Rate Onboard the MIR Station, *IEEE Transactions on Nuclear Science*, July 1997.
24. G. D. Badhwar, Radiation Measurements at the International Space Station Orbits, SAE 2001-01-2331, ICES-2001, Orlando, FL., July 2001.
25. D. Heynderickx, Comparison Between Methods to Compensate for the Secular Motion of the South Atlantic Anomaly, *Radiat. Meas.*, no. 26, pp. 369-373, 1996.

26. H. H. Heckman, G. H. Nakano, Low-Altitude Trapped Protons During Solar Minimum Period, 1962-1966, *J. Geophys. Research*, Vol. 74, no. 14, pp. 3575-3590, July 1969.
27. H. H. Heckman, G.H. Nakano, East-West Asymmetry in the Flux of Mirroring Geomagnetic Trapped Protons, *J. Geophys. Res.*, no. 68, pp. 2117-2120, 1963.
28. J. W. Watts, T. A. Parnell, H. H. Heckman, Approximate Angular Distribution and Spectra for Geomagnetically Trapped Protons in Low-Earth Orbit, Proc. *AIP Conference: High Energy Radiation in Space*, (ed. Rester, A. C., Jr. and Trombka, J. I.), pp. 75-85, 1989.
29. J. W. Kern, A Note on Vector Flux Models for Radiation Dose Calculations, *Radiation Meas.*, Vol. 23, no. 1, pp. 43-48, 1994.
30. K.A. Pfitzer, Radiation Dose to Man and Hardware as a Function of Atmospheric Density on the 28.5° Space Station orbit, *McDonnell Douglas Space Systems Co. Report No. H5387A*, Huntington Beach, CA, 1990.
31. G. D. Badhwar, Radiation Dose Rates in Space Shuttle as a Function of Atmospheric Density, *Radiat. Meas.*, no. 30, pp. 401-414, 1999.
32. R. C. Blanchard, W.N. Hess, Solar Cycle Changes in Inner Zone Protons, *J. Geophys. Res.*, no. 69, pp. 3927, 1964.
33. S. L. Huston, K.A. Pfitzer, Space Environment Effects: Low-Altitude Trapped Radiation Model, *NASA CR-1998-208593*, 1998.
34. D.F. Smart, M.A. Shea, Geomagnetic Transmission Functions for 400 km Altitude Satellite. *18th International Cosmic Ray Conference—Conference Papers MG Sessions*, Vol. 3, Tata Inst. of Fundamental Research (Colaba, Bombay), pp. 419-422, 1983.
35. C. Størmer, On the Trajectories of Electric Particles in the Field of a Magnetic Dipole with Applications to the Theory of Cosmic Radiation, *Astrophysica Norvegica*, Vol. II, no. 4, pp. 193-248, Jan. 1937.
36. D. J. Cooke, Geomagnetic-Cutoff Distribution Functions for Use in Estimating Detector Response to Neutrinos of Atmospheric Origin, *Phys. Rev. Letters*, Vol. 51, no. 4, pp. 320-323, July 1983.
37. D. F. Smart, M. A. Shea, Geomagnetic Cutoffs: A Review for Space Dosimetry Applications, *Adv. Space Research*, Vol. 14, pp. 787-796, Oct. 1994.
38. J. W. Wilson et al., Dynamic/Anisotropic Low Earth Orbit Environmental Model, *AIAA 2003-6221, Space 2003*, Long Beach, CA, Sept. 2003.
39. G.D. Badhwar, P.M. O'Neill, An Improved Model of Galactic Cosmic Radiation for Space Exploration Missions, *Nucl. Tracks Radiat. Meas.*, no. 20, pp. 427-410, 1995.
40. 1990 Recommendations of the International Commission on Radiological Protection, ICRP Publication 60, *Annals of the ICRP*, Vol. 21, Elsevier Science, N. Y., 1991.
41. C. P. Hugger, et al., Preliminary Validation of an ISS Radiation Shielding Model, *Proceedings of AIAA Space 2003 Conference*, AIAA 2003-6220, Long Beach, CA, 23-25 Sept. 2003.

REPORT DOCUMENTATION PAGE			Form Approved OMB No. 0704-0188		
<p>The public reporting burden for this collection of information is estimated to average 1 hour per response, including the time for reviewing instructions, searching existing data sources, gathering and maintaining the data needed, and completing and reviewing the collection of information. Send comments regarding this burden estimate or any other aspect of this collection of information, including suggestions for reducing this burden, to Department of Defense, Washington Headquarters Services, Directorate for Information Operations and Reports (0704-0188), 1215 Jefferson Davis Highway, Suite 1204, Arlington, VA 22202-4302. Respondents should be aware that notwithstanding any other provision of law, no person shall be subject to any penalty for failing to comply with a collection of information if it does not display a currently valid OMB control number.</p> <p>PLEASE DO NOT RETURN YOUR FORM TO THE ABOVE ADDRESS.</p>					
1. REPORT DATE (DD-MM-YYYY)		2. REPORT TYPE		3. DATES COVERED (From - To)	
01- 12 - 2006		Technical Publication			
4. TITLE AND SUBTITLE A Dynamic/Anisotropic Low Earth Orbit (LEO) Ionizing Radiation Model			5a. CONTRACT NUMBER		
			5b. GRANT NUMBER		
			5c. PROGRAM ELEMENT NUMBER		
6. AUTHOR(S) Badavi, Francis F.; West, Katie J.; Nealy, John E.; Wilson, John W.; Abrahms, Briana L.; and Luetke, Nathan J.			5d. PROJECT NUMBER		
			5e. TASK NUMBER		
			5f. WORK UNIT NUMBER		
7. PERFORMING ORGANIZATION NAME(S) AND ADDRESS(ES) NASA Langley Research Center Hampton, VA 23681-2199			8. PERFORMING ORGANIZATION REPORT NUMBER L-19312		
9. SPONSORING/MONITORING AGENCY NAME(S) AND ADDRESS(ES) National Aeronautics and Space Administration Washington, DC 20546-0001			10. SPONSOR/MONITOR'S ACRONYM(S) NASA		
			11. SPONSOR/MONITOR'S REPORT NUMBER(S) NASA/TP-2006-214533		
12. DISTRIBUTION/AVAILABILITY STATEMENT Unclassified - Unlimited Subject Category 93 Availability: NASA CASI (301) 621-0390					
13. SUPPLEMENTARY NOTES An electronic version can be found at http://ntrs.nasa.gov					
14. ABSTRACT The International Space Station (ISS) provides the proving ground for future long duration human activities in space. Ionizing radiation measurements in ISS form the ideal tool for the experimental validation of ionizing radiation environmental models, nuclear transport code algorithms, and nuclear reaction cross sections. Indeed, prior measurements on the Space Transportation System (STS; Shuttle) have provided vital information impacting both the environmental models and the nuclear transport code development by requiring dynamic models of the Low Earth Orbit (LEO) environment. Previous studies using Computer Aided Design (CAD) models of the evolving ISS configurations with Thermo Luminescent Detector (TLD) area monitors, demonstrated that computational dosimetry requires environmental models with accurate non-isotropic as well as dynamic behavior, detailed information on rack loading, and an accurate 6 degree of freedom (DOF) description of ISS trajectory and orientation.					
15. SUBJECT TERMS Ionizing radiation; Anisotropy; LEO; GCR; Rigidity; Trapped protons; Albedo neutrons					
16. SECURITY CLASSIFICATION OF:			17. LIMITATION OF ABSTRACT	18. NUMBER OF PAGES	19a. NAME OF RESPONSIBLE PERSON
a. REPORT	b. ABSTRACT	c. THIS PAGE			STI Help Desk (email: help@sti.nasa.gov)
U	U	U	UU	32	19b. TELEPHONE NUMBER (Include area code) (301) 621-0390